

ON THE BASIS FUNCTIONS WITH TRAVELING WAVE PHASE FACTOR FOR EFFICIENT ANALYSIS OF SCATTERING FROM ELECTRICALLY LARGE TARGETS

Z. Nie, S. Yan, S. He, and J. Hu

Department of Microwave Engineering
University of Electronic Science and Technology of China
No. 4, Sec. 2, N. Jianshe Rd., Chengdu, Sichuan 610054, P. R. China

Abstract—A basis function with the traveling wave phase factor, called as the phase extracted (PE) basis functions in this paper, has been applied for efficient solution of scattering from 3 dimensional (3-D) electrically large objects. In this paper, a rigorous derivation is given as a physical insight of this basis function. Defined on large patches and containing propagating wave phase dependence, this kind of bases exhibits very strong directivity, leading to a highly sparsed impedance matrix. Based on such observation, a matrix sparsification technique and an impedance prediction technique have been developed in this paper. The total memory requirement and computational time could be reduced significantly with methods proposed in this paper. The basic requirements of basis functions, i.e., current continuity and absence of charge accumulation are demonstrated, and the excellent behavior of PE basis functions in wideband applications has been summarized briefly. Several numerical examples have been given to show its good accuracy and high efficiency in solving scattering from electrically large complex objects.

1. INTRODUCTION

As the fast development of computational electromagnetic theory and computer technology, the ability of numerical codes for solving electromagnetic scattering has been remarkably improved. Traditionally, the Method of Moment [1–6] is very widely used in solving electromagnetic scattering and radiation problems. However,

the $O(N^2)$ computational and storage complexities prevent it from engineering application. Many efforts have been made to lower down the complexity of algorithm. The development of Multilevel Fast Multipole Algorithm (MLFMA) [7–15] makes both the memory requirement and computational complexity decrease to $O(N \log N)$. However, it is still difficult to solve some problems such as scattering from electrically extra large objects and radiation property of antennas equipped on large platform, because there are both electrically large structures and fine structures in these problems, each of them needs to be meshed with fine grid, leading to tremendous unknown number. As a fast algorithm, MLFMA does not reduce the number of the unknowns for a given problem.

In order to reduce the number of unknowns in EM calculation, many efforts focusing on new basis functions have been made since two decades ago. Some new basis functions which are either based on the analytical expressions or based on the numerical results have been developed.

In the newly developed basis functions, the most noticeable one is the higher order hierarchical basis functions based on modified Legendre polynomials [16, 17]. When the order is relatively high, the hierarchical basis functions can be defined on patches with the size as large as 2λ . However, the rising order also means the rapidly increasing number of basis functions in different orders. Actually, about 30 basis functions, along with the same number of unknown coefficients, are needed within one square wavelength on the smooth PEC surface. Furthermore, the iterative convergence became worse as the order rising.

Why the numbers of these well designed basis functions increase sharply when the patch is enlarged? This is because that those basis functions mentioned above have only the ability to describe the amplitude distribution of the current or the field, but have poor ability to represent the phase variation of the current in the definition domain. The variation of the current's phase is described only by the complex coefficients of basis functions. Obviously these coefficients, as the complex constants, have only very limited ability to express the phase distribution of surface current. To gain this ability, the number of basis functions on a unit area of the surface has to be maintained on a remarkable level.

Based on above understanding, it is expected that the number of basis functions can be reduced dramatically if some kind of basis functions with ability to describe the phase distribution of the induced current properly can be developed.

Some researches with similar ideas have been reported in the

recent decades [18–27]. To our knowledge, these works can be divided into two categories as follows.

The first kind of methods deals with the reconstruction of the induced currents. The researchers mainly use the idea that expresses the induced currents in carefully designed forms and calculate them at lower frequencies, then reconstruct them at the higher frequencies by using methods such as extrapolation or numerical extraction. The representative works include [18, 19] and [20]. The second kind of methods involves some new basis functions with the phase term in numerical analysis to enlarge their definition domain [21–27].

In this paper, all the above mentioned basis functions will be termed as “Phase Extracted Basis Functions”, regardless what was termed in each of these works. To have a better physical insight, a theoretical derivation is given to show the traveling wave phase dependence of the induced current on the smooth surface of PEC targets as a physical explanation of such kind of basis functions. Although such basis functions could be defined on larger patches than conventional ones due to the phase term involved, the numerical evaluation of impedance elements is still a serious problem. Since it still needs the entire PEC surface to be integrated and tested. Due to the fast oscillatory property of the integral kernel, remarkable number of quadrature points should be maintained at the integral domain, leading to almost the same computational cost as the standard MoM. In [20], the far-field approximation is used to alleviate this problem. In this paper, differently, a matrix sparsification technique is introduced to save the memory requirement of storing the whole impedance matrix. An impedance prediction technique is also introduced to significantly reduce the computational time of evaluating the impedance elements. It is also demonstrated that the new basis functions satisfy the basic requirement of the bases, i.e., current continuity and absence of the charge accumulation. Furthermore, the excellent behavior of PE bases for wideband applications has been discussed and summarized briefly.

In Section 2, the rigorous deduction of phase dependence of induced current on the PEC surface is presented. The PE basis functions are reviewed in Section 3. The proof of the charge-free characteristic for PE basis functions is also given in Appendix. In Section 4 the implementation of PE basis functions in MoM solutions of integral equations is presented. The radiation characteristic of PE basis functions is investigated. A matrix sparsification technique and an impedance prediction technique are introduced to reduce the memory and computational cost of the moment method. Numerical examples are given in Section 5 to illustrate the good accuracy and high efficiency of this method. After some discussions and brief summary for the

advantage of the PE bases in Section 6, the conclusion is given in Section 7.

2. THE TRAVELING WAVE PHASE DEPENDENCE OF THE INDUCED CURRENT ON PEC SURFACE

In order to deduce the phase dependence of the induced surface current on the PEC surface, we begin with the Maxwell's equation:

$$\nabla \times \mathbf{E} = i\omega\mu\mathbf{H}, \quad (1)$$

the surface equivalence theorem:

$$\mathbf{J} = \hat{\mathbf{n}} \times \mathbf{H}, \quad (2)$$

and the constitutive relation:

$$\mathbf{D} = \varepsilon\mathbf{E} \quad (3)$$

The induced current has the following relationship with electric flux from above expressions:

$$\mathbf{J} = \frac{1}{i\omega\mu\varepsilon} \hat{\mathbf{n}} \times \nabla \times \mathbf{D}, \quad (4)$$

where ε and μ are constant in homogeneous background media. Curl \mathbf{D} can then be expressed in the local coordinate as:

$$\nabla \times \mathbf{D} = \left(\nabla_t + \hat{\mathbf{n}} \frac{\partial}{\partial n} \right) \times (\mathbf{D}_t + \hat{\mathbf{n}} D_n) = \nabla_t \times \mathbf{D}_t + \nabla_t \times \hat{\mathbf{n}} D_n + \hat{\mathbf{n}} \times \frac{\partial \mathbf{D}_t}{\partial n} \quad (5)$$

where $\hat{\mathbf{n}}$ stands for the normal direction of the PEC surface at any given point \mathbf{r} , D_n and \mathbf{D}_t are normal component and tangential component of electric flux, respectively.

Note that $\nabla_t \times \mathbf{D}_t = 0$ because the partial derivative is taken on the object's surface where $\mathbf{D}_t \equiv 0$ due to the boundary condition at PEC surfaces. Hence,

$$\mathbf{J} = \frac{1}{i\omega\mu\varepsilon} \left(\nabla_t D_n - \frac{\partial \mathbf{D}_t}{\partial n} \right) \quad (6)$$

Taking the surface divergence on both sides of (6), and considering the boundary condition of PEC

$$D_n = \rho_s, \quad (7)$$

and the continuity condition of current:

$$\nabla_t \cdot \mathbf{J} = i\omega\rho_s, \quad (8)$$

we have

$$\nabla_t \cdot \mathbf{J} = i\omega\rho_s = \frac{1}{i\omega\mu\varepsilon} \left(\nabla_t^2 \rho_s - \nabla_t \cdot \frac{\partial \mathbf{D}_t}{\partial n} \right) \quad (9)$$

Therefore,

$$\nabla_t^2 \rho_s + k^2 \rho_s = \nabla_t \cdot \frac{\partial \mathbf{D}_t}{\partial n} \quad (10)$$

Equation (10) is an inhomogeneous scalar Helmholtz equation that surface charge should satisfy. Its solution can be expressed as the summation of the general solution of the corresponding homogeneous equation and a particular solution of this inhomogeneous equation.

2.1. The General Solution of the Homogeneous Equation

By solving the homogeneous equation

$$\nabla_t^2 \rho_s + k^2 \rho_s = 0, \quad (11)$$

one can construct the solution with following form:

$$\rho_s = C_m e^{i\mathbf{k}^m \cdot \mathbf{r}}, \quad (12)$$

where \mathbf{k}^m is a vector which amplitude equals to k . Note that in the local rectangular coordinate system $(\hat{\mathbf{u}}, \hat{\mathbf{v}}, \hat{\mathbf{w}})$, where $\hat{\mathbf{w}} = \hat{\mathbf{u}} \times \hat{\mathbf{v}}$ is the outward unit normal:

$$\mathbf{k}^m = (k_u^m, k_v^m, k_w^m) \quad (13)$$

$$\mathbf{r} = (u, v, w) \quad (14)$$

Submitting (12) into (11):

$$- \left[(k_u^m)^2 + (k_v^m)^2 \right] C_m e^{i\mathbf{k}^m \cdot \mathbf{r}} + k^2 C_m e^{i\mathbf{k}^m \cdot \mathbf{r}} = 0 \quad (15)$$

Therefore,

$$(k_u^m)^2 + (k_v^m)^2 = k^2 \quad (16)$$

$$k_w^m = 0 \quad (17)$$

Finally, the general solution of this homogeneous equation can be expressed as:

$$\rho_s(\mathbf{r}) = \sum_{m=1}^M C_m e^{i\mathbf{k}_t^m \cdot \mathbf{r}}, \quad (18)$$

where $\|\mathbf{k}_t^m\| = k = \omega\sqrt{\mu\varepsilon}$, and its direction could be any tangential direction of the PEC surface.

As is well known, the above homogeneous solution does not corresponding to the excitation condition. Therefore it can be considered as the eigenmode (resonance mode) independent of the excitation.

2.2. The Particular Solution of the Inhomogeneous Equation

According to the boundary condition on PEC surfaces,

$$\mathbf{D}_t(\mathbf{r})|_{\mathbf{r}\in\text{PEC}} = \mathbf{D}_t^{\text{inc}}(\mathbf{r})|_{\mathbf{r}\in\text{PEC}} + \mathbf{D}_t^{\text{sca}}(\mathbf{r})|_{\mathbf{r}\in\text{PEC}} \equiv 0 \quad (19)$$

Note that the tangential component of incident electric flux has the traveling wave phase dependence which can be expressed as $\mathbf{D}_t^{\text{inc}}(\mathbf{r})|_{\mathbf{r}\in\text{PEC}} \sim e^{i\mathbf{k}^i\cdot\mathbf{t}}$. Due to the phase matching condition implied in (19), the tangential component of scattering electric flux has the same phase dependence $\mathbf{D}_t^{\text{sca}}(\mathbf{r})|_{\mathbf{r}\in\text{PEC}} \sim e^{i\mathbf{k}^i\cdot\mathbf{t}}$ along the PEC surface. So the tangential component of the total \mathbf{D} flux and its partial derivative also have such phase dependence:

$$\mathbf{D}_t(\mathbf{r})|_{\mathbf{r}\in\text{PEC}} \sim e^{i\mathbf{k}^i\cdot\mathbf{t}} \quad (20)$$

$$\nabla_t \cdot \frac{\partial \mathbf{D}_t}{\partial n} \sim e^{i\mathbf{k}^i\cdot\mathbf{t}} \quad (21)$$

Hence, the right hand side (RHS) of the inhomogeneous Equation (10) has the phase dependence of traveling wave. It is easy to figure out that ρ_s with the same phase dependence of the RHS *could* be a particular solution of the inhomogeneous equation, which can be expressed as:

$$\rho_s(\mathbf{r}) \sim e^{i\mathbf{k}^i\cdot\mathbf{t}} \quad (22)$$

2.3. The Phase Dependence of the Induced Sources

The general solution of (10) can be written as:

$$\rho_s(\mathbf{r}) = \sum_{m=1}^M C_m e^{i\mathbf{k}_t^m\cdot\mathbf{t}} + D(\mathbf{r}) e^{i\mathbf{k}^i\cdot\mathbf{t}} \quad (23)$$

Due to relationship (8), the induced surface current \mathbf{J} has the same phase dependence.

2.4. Discussions

1. The homogeneous solutions are the Eigen solutions, which are decided by the geometry shape of the object, and are independent to excitation condition.
2. This inhomogeneous solution is caused by excitation, including the incident angle and operating frequency.
3. If the shape of object was smooth and convex, the first term of (23) could be neglected and the second term is dominant. However, if there were many edges, corners, or even cavities involved in the object, the first term of (23) turn out to be important and could not be neglected.

3. PHASE EXTRACTION BASIS FUNCTIONS

For smooth and convex problems, the particular solution of the inhomogeneous equation is dominant. So we can just consider the propagating wave phase factor in the induced current:

$$\mathbf{J} \sim e^{i\mathbf{k}^i \cdot \mathbf{r}} \quad (24)$$

As the induced current on the PEC surface has the traveling wave phase property, the basis functions, which will approximate the induced surface current, can be expressed as the multiplication of two factors: the amplitude factor and the phase factor. Considering its accuracy in representing arbitrary curvilinear surfaces, the curvilinear triangular patches are used to discretize the surface of scatterer, and CRWG (curvilinear RWG) functions [28–31] is chosen as the amplitude term of the PE basis functions in this paper because of its excellent performance, while the phase factor is an exponential function as shown in (24). Thus

$$\mathbf{J}(\mathbf{r}) = \mathbf{j}(\mathbf{r})e^{i\mathbf{k}^i \cdot \mathbf{r}} \quad (25)$$

where $\mathbf{j}(\mathbf{r})$ is the unknown amplitude factor, which can be approximated as the superposition of CRWG basis functions:

$$\mathbf{j}(\mathbf{r}) = \sum_{n=1}^N a_n \mathbf{j}_n(\mathbf{r}) \quad (26)$$

where $\mathbf{j}_n(\mathbf{r})$ is CRWG basis functions, $e^{i\mathbf{k}^i \cdot \mathbf{r}}$ is the analytic phase factor. Apparently, the phase shift between two adjacent points on the surface is determined by the propagation factor equal to the space projection of the incident wave number in the direction tangential to the surface.

Multiplying the phase term, the phase extracted basis functions can be finally constructed and the induced current can be expanded with the phase extracted basis functions $\mathbf{j}_n(\mathbf{r})e^{i\mathbf{k}^i \cdot \mathbf{r}}$:

$$\mathbf{J}(\mathbf{r}) = \sum_{n=1}^N a_n \mathbf{j}_n(\mathbf{r}) e^{i\mathbf{k}^i \cdot \mathbf{r}} \quad (27)$$

Mathematically speaking, after the phase extraction, the residual part of the bases only needs to express the amplitude distribution. So the requirement to the amplitude factor is abated greatly.

Applying Gauss divergence theorem, it is easy to prove that, the phase extracted basis functions are free of charge accumulation. The detailed proof can be found in the appendix of this paper.

4. IMPROVE MOM WITH THE PE BASIS FUNCTIONS

4.1. Implementation of MoM

There are no big differences in the implementation of Moment Method between using PE basis functions and conventional CRWG basis. The PE basis functions are substituted into integral equations and the Galerkin's method is used ($\mathbf{t}_m(\mathbf{r})e^{i\mathbf{k}^i \cdot \mathbf{r}}$ is used as the test function) in the testing procedure to discretize the integral equations.

Considering Electric Field Integral Equation (EFIE) for example, the solution procedure is as follows. The EFIE

$$\int_{S'} \left[g(\mathbf{r}, \mathbf{r}') \mathbf{J}(\mathbf{r}') + \frac{1}{k^2} \nabla g(\mathbf{r}, \mathbf{r}') \nabla' \cdot \mathbf{J}(\mathbf{r}') \right] d\mathbf{r}' = \frac{4\pi i}{k\eta} \mathbf{E}^{inc}(\mathbf{r}) \quad (28)$$

can be discretized in the way mentioned above to obtain the matrix equation

$$\sum_{n=1}^N Z_{mn} a_n = V_m \quad m = 1, 2, \dots, N \quad (29)$$

In this matrix equation, the expression of matrix element is

$$Z_{mn} = \int_S \int_{S'} g e^{i\mathbf{k}^i \cdot (\mathbf{r}' - \mathbf{r})} \left[\mathbf{t}_m \cdot \mathbf{j}_n - \hat{\mathbf{k}}^i \cdot \mathbf{t}_m \hat{\mathbf{k}}^i \cdot \mathbf{j}_n - \frac{i}{k} \left(\nabla \cdot \mathbf{t}_m \hat{\mathbf{k}}^i \cdot \mathbf{j}_n - \hat{\mathbf{k}}^i \cdot \mathbf{t}_m \nabla' \cdot \mathbf{j}_n \right) - \frac{1}{k^2} \nabla \cdot \mathbf{t}_m \nabla' \cdot \mathbf{j}_n \right] d\mathbf{r}' d\mathbf{r}, \quad (30)$$

and the excitation vector is

$$V_m = \frac{4\pi i}{k\eta} \int_S \mathbf{t}_m \cdot \hat{\mathbf{e}}_i d\mathbf{r} \quad (31)$$

In (30), $g = e^{ik|\mathbf{r}-\mathbf{r}'|}/|\mathbf{r}-\mathbf{r}'|$ is the scalar Green's function in free space, \mathbf{r} and \mathbf{r}' are the field point and source point, respectively. In (31), $\hat{\mathbf{e}}_i$ is the polarization vector of the incident waves.

One point should be noted is that, no matter how large the grid patch could be when use PE bases, the numerical integration still needs the entire PEC surface to be integrated and tested. Due to the fast oscillatory property of the integral kernel, remarkable number of quadrature points should be maintained at the integral domain as other integration that involves high oscillatory kernel [20], leading to almost the same computational cost as the standard MoM. One way to alleviate this problem is to use far-field approximation in the evaluation of matrix elements, just as [20] has done. Differently, in this paper we use a matrix sparsification technique and an impedance element prediction technique to alleviate the huge resource expense.

4.2. Radiation Characteristics of PE Bases

Examining the impedance matrix generated by phase extracted basis/test functions defined on large triangular patches, one can find out that the impedance matrix can be sparsified by setting a threshold. To describe this property of the matrix, consider a PEC sphere with radius of 1.0m. The frequency of incident wave is 3.0GHz, and the mesh size is about 0.125m, i.e., 1.25λ (3528 unknowns are needed). Figure 1 is a linear grayscale colormap showing the amplitude distribution of impedance matrix obtained by the combined field integral equation (CFIE), where PE-CRWG functions are used as both

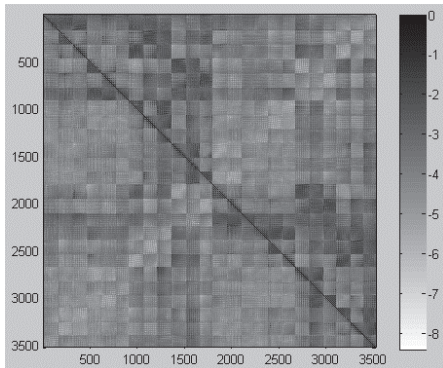


Figure 1. A linear grayscale colormap of the impedance matrix.

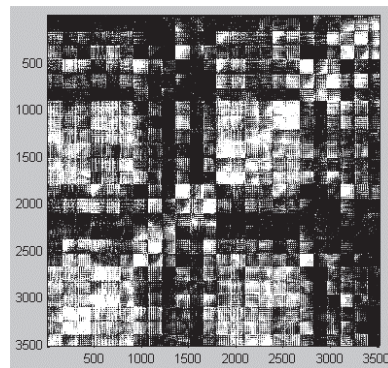


Figure 2. The threshold = 0.0001. Percentage of zeros = 33.51%.

basis and test functions. In this figure, the horizontal axis is the index of basis functions while the vertical one is the index of test functions. The tick label of the color bar at the right side of the figure is defined as (32), where z_{ji} is the complex impedance element obtained by j th test function and i th basis function. The meaning of this definition is clear: each element of the matrix is firstly normalized by its column, and then the logarithm (base 10) of this “normalized norm” is taken:

$$label = \lg \left(\frac{\|z_{ji}\|}{\max_{j=1}^N \|z_{ji}\|} \right), \quad i, j = 1 \dots, N \quad (32)$$

By setting different thresholds, this impedance matrix can be sparsified. Elements that satisfy

$$\|z_{ji}\| < threshold \cdot \max_{j=1}^N \|z_{ji}\| \quad (33)$$

are neglected and set to zero.

Figures 2, 3, and 4 show the sparse matrices in black and white colormap according to different thresholds. The impedance terms whose normalized norms are smaller than the threshold are shown in white, while the rest are in black. The sparsities, i.e., the percentages of zeros, are 33.51%, 78.73%, and 96.51%, under the thresholds chosen as 0.0001, 0.001, and 0.01, respectively. It can be seen directly from

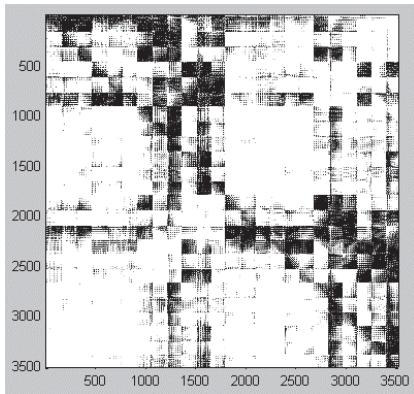


Figure 3. The threshold = 0.001. Percentage of zeros = 78.73%.

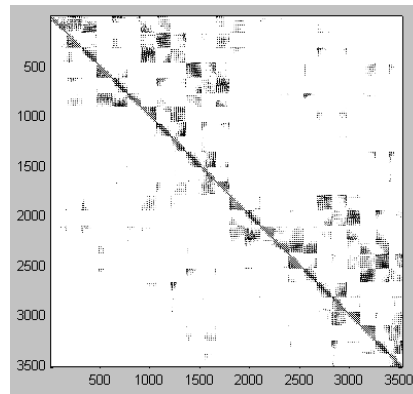


Figure 4. The threshold = 0.01. Percentage of zeros = 96.51%.

these figures that the phase extracted bases can generate very sparse impedance matrix provided a reasonable threshold is set.

In fact, some other bases such as wavelet bases and higher order hierarchical bases also generate sparse matrices after setting a threshold. Wagner and Chew [32] explained this phenomenon in terms of radiation/receiving characteristics by calculating the basis functions' spatial spectrum distribution using Fourier transformation.

In this paper, the physics behind the sparsification of the matrix is discussed also by the radiation/receiving characteristics of the basis functions. The difference with [32] is that the radiation pattern is generated by a traveling wave aperture distribution rather than a standing wave aperture distribution. The conventional bases, without the phase information, can only be considered as apertures with uniform phase distribution, i.e., standing wave aperture. For most targets with convex surfaces, the mutual coupling directions rarely fall into the major lobe's direction of the radiation basis. Therefore, the difference of coupling strength from different directions is not very significant. Contrarily, the PE bases can be seen as traveling wave apertures distribution since they have the analytic phase distribution the same as incident wave. Hence, the major lobe's direction is no longer the normal direction of the aperture, but somehow leans to the direction in which the phase delays. This leads to the strong mutual coupling in some directions but very weak coupling in other directions, i.e., the "contrast" of coupling strength from different directions is significant. As a result, there might be some very small elements that can be neglected.

4.3. Matrix Sparsification Technique

In the conventional MoM, the memory requirement is $O(N^2)$, where N is the number of unknowns. Although the PE bases can reduce the unknowns dramatically, due to the high storage complexity, the memory requirement still augments rapidly while N increases. However, the actual storage requirement can be expressed as aN^2 , while a is the coefficient determined by the exact approach in the implementation of MoM.

Utilizing the sparse matrix generated by PE bases defined on large patches can alleviate the large storage requirement by means of reducing the coefficient a to a small value. By setting a threshold, it can be reduced to about 10% of the original one if the percentage of non-zero elements is 10% for example, leading to 90% memory saving.

To determine which element can be neglected, the rigorous criterion is (33). However, in the real application, it is not efficient because all elements in a column have to be considered. For

convenience, the following expression is used as the criterion in the actual implementation of MoM:

$$\|z_{ji}\| < threshold \cdot \|z_{ii}\| \quad (34)$$

In (34), z_{ii} is the self impedance term of the i th column. Following this criterion, elements only need to be compared with the self impedance term which can be calculated beforehand. Elements satisfying (34) will be neglected and not stored in the memory. By this means, the memory requirement is decreased.

The property variations after thresholding are examined here. The numerical model utilized is the PEC sphere with radius of 1.0 m. 2352 curvilinear triangles, with patch length of about 0.125 m, are used to discretize this sphere, resulting in 3528 unknowns when PE-CRWG bases are employed. All results are obtained by CFIE. Figure 5, shown with double y axes, illustrates memory savings as well as precision losses as functions of threshold at the same frequency of 3000 MHz. The left y axis is the RMS error (solid line with squares) between the calculated data and Mie series following expression (35), while the right one shows memory requirement (dotted line with triangles) and percentage of non-zero elements (dotted line with stars). The definition of RMS error is:

$$RMS = \sqrt{\frac{\sum_{n=1}^N |\sigma_n^{cal} - \sigma_n^{ref}|^2}{N}} \quad (35)$$

where N is the number of scattering angles, σ_n^{cal} and σ_n^{ref} are the calculated RCS and reference RCS at the n th scattering angle, respectively.

It can be found from Figure 5 that, at the same frequency of 3000 MHz, as threshold increases (from 0.000 to 0.010), the percentage of non-zeros, as well as the memory requirement, decreases, at the same time, the RMS error increases a little. When the threshold chosen as 0.000, i.e., the full matrix is used to solve integral equation, 95.54 Mb memories is needed. However, when threshold is set as 0.005, only 10.36 Mb is needed. And this number decreases further to 5.58 Mb when the threshold is set as 0.010. Generally speaking, the percentage of non-zero elements decreases to less than 10% and memory requirement less than 16% of the original one when the threshold chosen is greater than 0.003. At the same time, the RMS error is less than 0.70 dB when the threshold is smaller than 0.007. Considering these conflicting factors (memory saving and precision

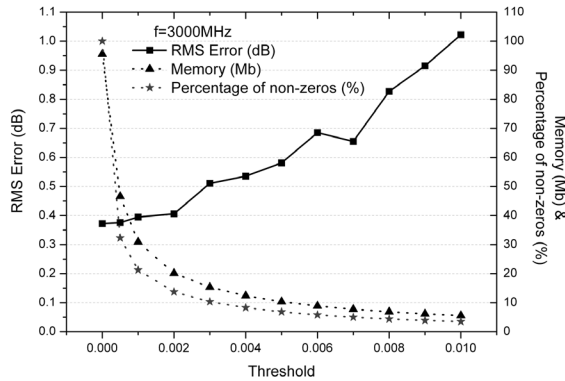


Figure 5. Curves of property variations as functions of the threshold at the same frequency of 3000 MHz.

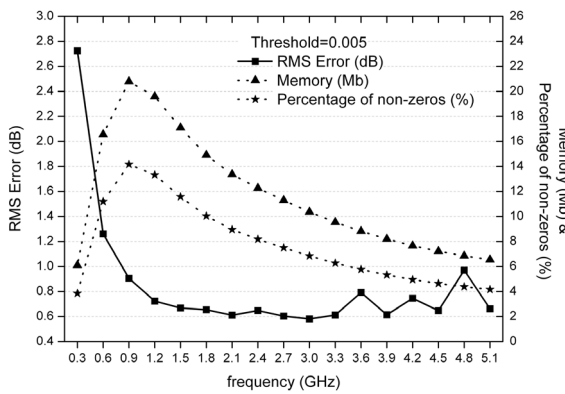


Figure 6. Curves of property variations as functions of frequency at the same threshold of 0.005.

loss), the advisable value of the threshold may be chosen between 0.003 and 0.007.

Figure 6, also shown with double y axes, demonstrates the memory savings and precision losses as functions of frequency when the same threshold 0.005 is chosen. The vertical axes settings are the same as Figure 5, and the horizontal axis is the frequencies from 0.3 GHz to 5.1 GHz. In this figure, the percentage of non-zeros, proportional to the memory requirement, decreases with frequency after 0.9 GHz, and are less than 14% in the whole range of considered frequencies. On the other hand, as the frequency increases, the RMS error shows a

decreasing tendency. In the frequency range from 1.2 GHz to 5.1 GHz (corresponding patch length of about 0.5λ to 2.125λ), the RMS error remains between 0.6–0.8 dB, except at 4.8 GHz. Because the same mesh grid obtained at the lowest frequency (0.3 GHz) is used for all frequencies, the electrical patch length becomes larger and larger as the frequency rises. Therefore, the RMS error has a little increase at 3.6 GHz, 4.2 GHz and 4.8 GHz. But the error continues to decrease after these frequencies. At the highest frequency of 5.1 GHz (where the electrical radius of the sphere is 17λ , and patch length about 2.125λ), the percentage of non-zeros is 4.17%, with the storage requirement of only 6.55 Mb, while the RMS error is acceptable at 0.66 dB.

From the discussions in this subsection, the following observations can be made:

- (1) The RMS error increases and memory requirement (along with matrix sparsity) decreases when raising the threshold under same frequency;
- (2) The RMS error, as well as the memory requirement and matrix sparsity, decreases when frequency rises under same threshold.

In summary, 0.005 may be a good choice of threshold and larger patch (1.0λ to 2.0λ) is preferred in order to obtain a satisfying result. Although they may not be the optimal values for all objects, they are at least safe values to be applied. This conclusion can be obtained by means of comparing the mutual coupling level of different objects. As a symmetric convex object with smooth surface, the mutual coupling level of sphere is relatively low compared with other complicated objects, especially some real engineering targets. If a same threshold (0.005, for example) is applied in both sphere and an engineering target, the neglected elements of sphere will be much more than the latter one. In this situation, if the result of sphere is still satisfying, that of the engineering target should be acceptable. In the section of numerical examples, these values are applied in two engineering targets, and nice results are obtained. The sparsities under the threshold 0.005 of these two objects indicate that above discussion is reasonable.

4.4. Impedance Element Prediction Technique

It is shown in the previous subsection that the memory requirement can be reduced significantly while maintaining the calculation precision by using the matrix sparsification technique. However, in order to decide which elements could be neglected and which should be reserved, every impedance element need to be calculated accurately. Hence, the time consuming for calculating the impedance matrix is not abated at all in

the matrix sparsification technique. Although the time requirement for matrix-vector multiplication in solving the matrix equation is shortened, it still takes a long time to finish the total computation.

In this subsection, an impedance element prediction technique is presented to further reduce the time consuming in the impedance integration.

In the accurate integration of the impedance term, several Gaussian quadrature points (4 or 7, for example) are needed on each triangle. Therefore, to finish integration on a test/basis triangle pair, 16 or 49 points are used in total. In the prediction technique, however, one point Gaussian integral formula is used.

The calculation steps are as follows:

- (1) Use one point Gaussian quadrature formula to predict a rough value of an impedance term;
- (2) The predicted elements, which are less than the threshold, are neglected;
- (3) Those are larger than the threshold are calculated again in the accurate way (4 or 7 points Gaussian quadrature formula), and compare again with the threshold;
- (4) The elements which are larger than the threshold in the second comparison are reserved and stored in the memory.

To validate the efficiency of this method, the numerical model in the previous subsection is considered again.

First, scattering at the frequency of 3.0 GHz is calculated with different thresholds with/without the prediction of impedance elements. Figures 7, 8, and 9 demonstrate the results.

Figure 7 examines the percentage of non-zero elements obtained from direct (non-predicted) method and predicted method, respectively. The black solid line with squares is the result from the non-predicted MoM, and the grey dotted line with circles is obtained by the predicted MoM. It is shown that the two curves match with each other very well, exhibiting a very good prediction precision of this technique. Figure 8 compares the RMS errors between these two approaches. It is observed that the calculation precision does not have a significant loss compared with the results gained by non-predicted ones.

With the good prediction precision for impedance terms and calculation accuracy for RCS, Figure 9 exhibits a very attractive predominance of the prediction technique in saving the total computational time. Without impedance prediction, the time consumed is about 10 hours for all thresholds. But it falls to only about 2 hours after impedance prediction when the threshold is 0.005.

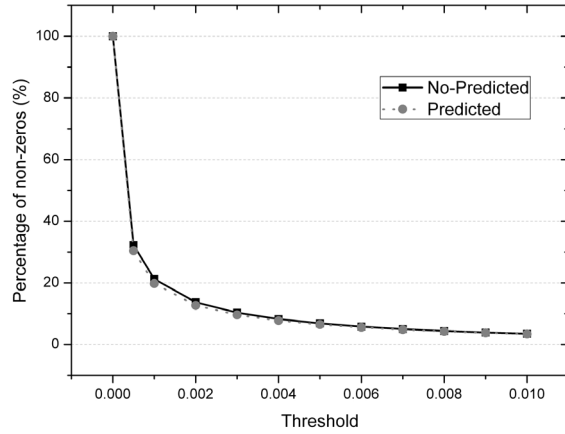


Figure 7. Comparison of percentage of non-zeros between predicted and not predicted methods at the frequency of 3000 MHz.

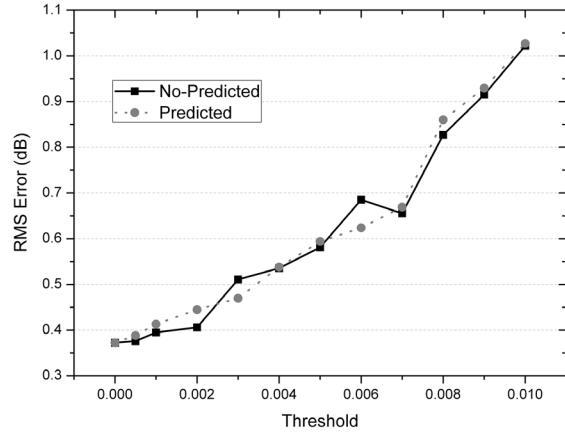


Figure 8. Comparison of RMS errors between predicted and direct methods at the frequency of 3000 MHz.

If the threshold is chosen as 0.01, the total computational time is only 1 hour.

Secondly, scattering under the same threshold of 0.005 is calculated at different frequencies with/without the prediction of impedance elements. Results are shown in Figures 10, 11, and 12. Similar conclusions can be made from these three figures: analogous percentage of non-zeros between predicted and non-predicted methods,

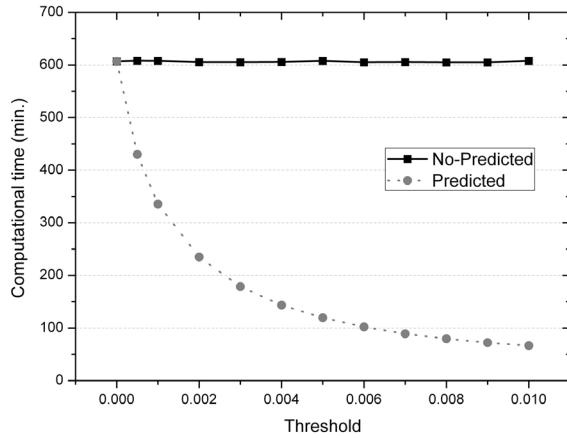


Figure 9. Comparison of computational time between predicted and direct methods at the frequency of 3000 MHz.

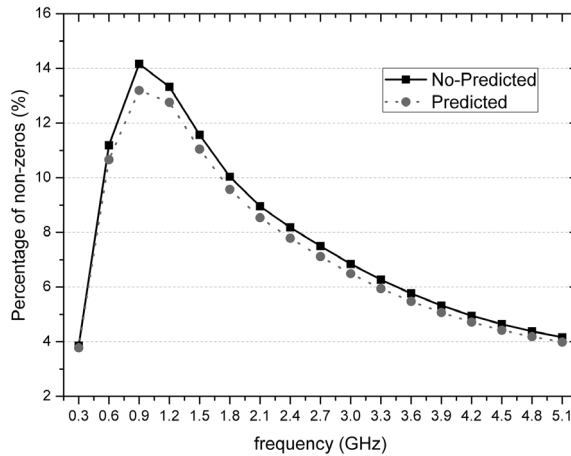


Figure 10. Comparison of percentage of non-zeros between predicted and direct methods under the threshold of 0.005.

the RMS error, as well as great computational time saving. Moreover, from Figure 11, it is surprising that, the results obtained by the predicted method are even better than non-predicted ones at frequencies 4.2 GHz to 5.1 GHz, especially at 4.8 GHz, exhibiting some robust property of the prediction technique. From Figure 12, we observe that the computational time saving in the whole range from 0.3 to 5.1 GHz is about 4 to 6 times, under the threshold chosen as

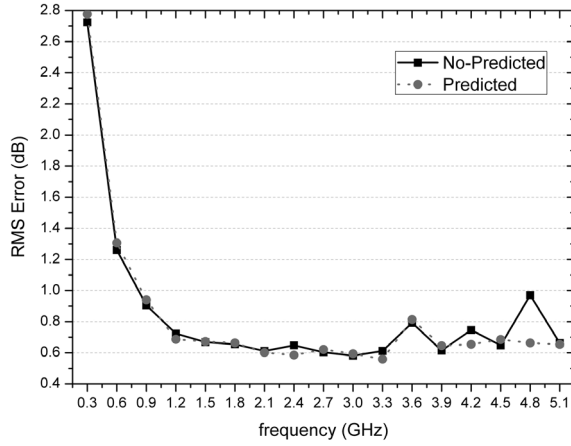


Figure 11. Comparison of RMS errors between predicted and direct methods under the threshold of 0.005.

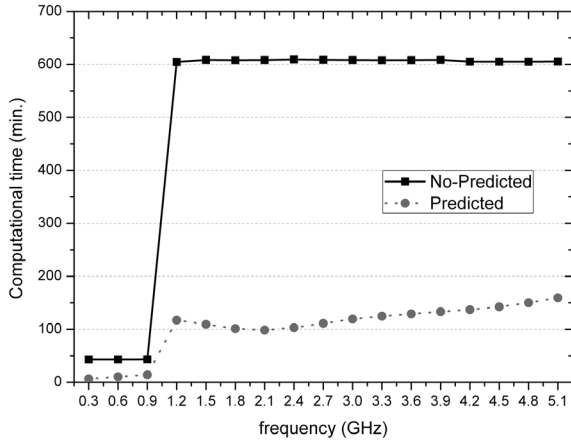


Figure 12. Comparison of computational times between predicted and direct methods under the threshold of 0.005.

0.005. The step change of CPU time occurred at 1.2 GHz, which is caused by the automatic quadrature points refining.

From these six figures and discussions in this subsection, it is attested that the impedance prediction technique can reduce the computational time significantly while maintaining a given computational accuracy.

5. NUMERICAL EXAMPLES

In this section, three numerical examples are given to show the dramatic superiority and the reliable precision of the solution by use of the PE basis functions.

The first example is the scattering from a PEC sphere with radius of 1.0 m. Figure 13 shows the bistatic RCS and phase distribution under the frequency of 3.0 GHz. The mesh density is about 0.125 meter. That is to say, the patch size is about 1.25λ at the operation frequency. In this figure, solid lines are analytic solution of Mie series, and dashed lines are obtained by the PE basis functions. For comparison, Figure 14 gives the RCS calculated by CRWG basis functions under the same mesh grid. It is very clear that, the results from PE basis function and from Mie series are in very good agreement with each other (the RMS error is only 0.6586 dB), while that from traditional CRWG bases are totally wrong.

Table 1. Comparison of computational data for sphere under 3.0 GHz.

Sphere ($f = 3.0$ GHz) (CFIE)	Unknown	Sparsity (%) / Threshold	Total Iteration Step	Total Memory Requirement (Mb)	Total Computational Time (min.)
PE-MoM	3,528	93.51 / 0.005	9	9.64	97.45
CRWG-MLFMA	285,768	—	21	1,213.22	165.88
Improvement Ratio	81.0	—	—	125.85	1.70

Table 1 represents the comparison of computational data under 3.0 GHz. In this table, the number of unknowns, the sparsity of the impedance matrix when sparsification technique is used, the total iteration step in GMRES method, the total memory requirement, and the total computational time are given for PE-MoM and CRWG-MLFMA (the results are not shown here), respectively. The improvement ratios of the PE-MoM are also listed in this table. It is easy to see that, all items have been reduced dramatically with the phase extraction method even compared with MLFMA.

The second example is scattering from a missile-like object with the length of 23.04λ . The total length of this target is 0.864 m, and the frequency is 8.0 GHz. Figure 15 shows the geometry shape of the missile-like target which lies along the z -axis. The incident wave comes from the x direction and is polarized along the z direction. Figure 16 compares the results from MLFMA using conventional CRWG bases

(the black solid line) and that from the method of moments using PE-CRWG bases (the red dashed line). In this figure, two curves agree with each other very well except at 90° and 270° , which correspond to the directions of tail and nose of the target, respectively, and may be caused by the edge current which is unable to be described with the bases defined on the large patches.

Table 2 summarizes the computational data for MoM and

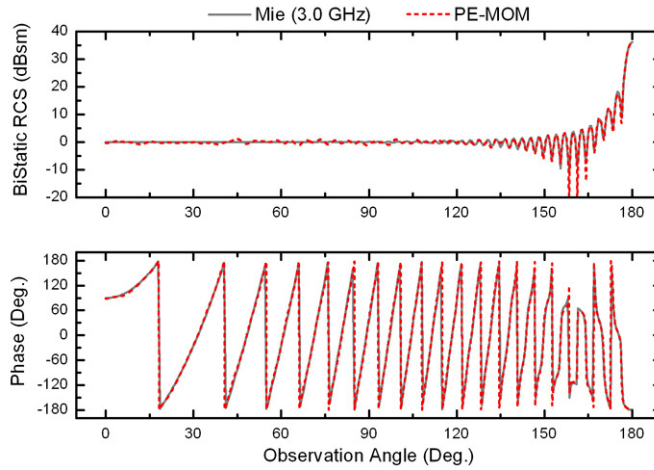


Figure 13. Bistatic RCS of a sphere under 3.0 GHz. PE bases used.

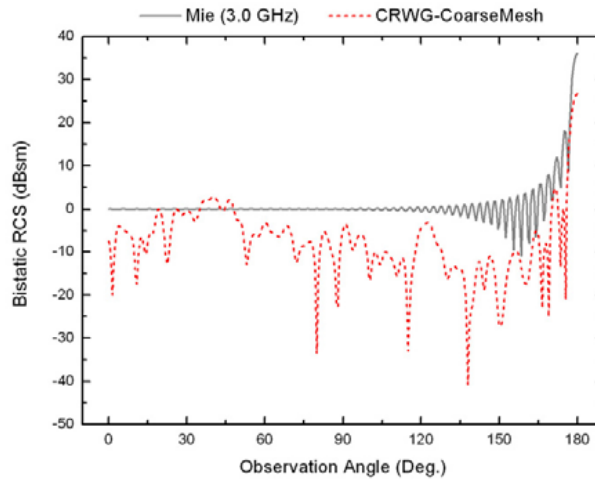


Figure 14. Bistatic RCS obtained by CRWG bases under the same mesh grid as PE bases.



Figure 15. Geometry model of a missile-like object.

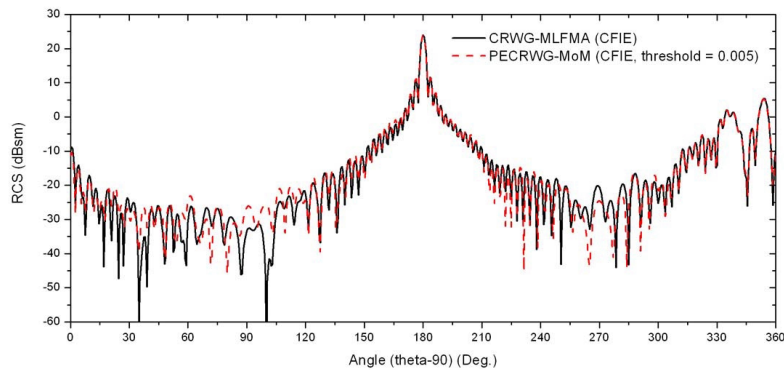


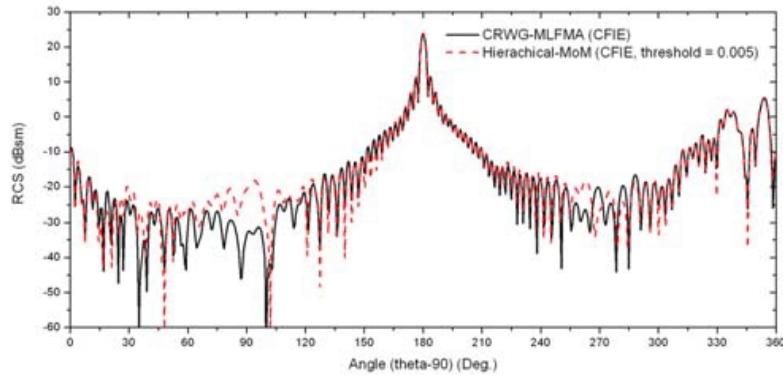
Figure 16. Bistatic RCS of a missile-like target. The frequency is 8.0 GHz and electrical size of the target is 23.04λ . HH -polarized.

MLFMA in calculating this missile-like object. The mesh grid is as large as 1λ for using the phase extracted bases, while it is 0.125λ for non-extracted ones. In other words, PE bases cause 58.39 times saving of the number of unknowns. In the MoM solution, the matrix sparsification technique, as well as the impedance element prediction technique, is used and the threshold is chosen as 0.005, leading to 94.50% zero elements in the impedance matrix. The use of PE bases made the performance of MoM much more excellent than traditional MLFMA, i.e., dramatically saving in both memory requirements (355.30 times saving) and CPU time cost (17.55 times saving). At the same time, it only takes 30 steps to converge to a residual error of 0.001 when the CG iteration method is used, while the MLFMA needs 113 steps.

Figure 17 provides the comparison data obtained from the maximally orthogonalized higher order hierarchical basis functions [6, 7]. Under the mesh size of about 1λ , there are only 548 curvilinear quad-

Table 2. Comparison of computational data for Figure 16.

Missile-Like ($f = 8.0$ GHz) (CFIE)	Unknown	Sparsity (%) / Threshold	Total Iteration Step	Total Memory Requirement (Mb)	Total Computational Time (hr.)
PE-MoM	3,552	94.50 / 0.005	30	8.56	1.18
CRWG-MLFMA	207,408	—	113	3,041.37	20.71
Improvement Ratio	58.39	—	—	355.30	17.55

**Figure 17.** Result for comparison. The red dashed line is obtained from the higher order hierarchical bases.

ranges obtained. However, due to the use of 3 order hierarchical basis functions, the final number of basis functions is 9864. Although the threshold of the higher order hierarchical basis functions is also chosen as 0.005, it only leads to the percentage of zeros of 29.80%, far less than the 5.50% of PE bases. At a result of the number of unknowns and sparsity, the total memory requirement is about 276.50 Mb, about 32.30 times of that needed by PE bases. Moreover, from Figure 17, we can point out the significant disagreements at the angle ranges from 60° to 100° , and from 250° to 280° , which strongly support our explanation that the errors are caused by the use of large patches.

The third example is the scattering from a plane-like target shown in Figure 18. The total length of this model plane is 11.0 m and it lies on the xoy plane. The concerned frequency is 3.0 GHz, which means the total length of this target is 110λ . Under HH polarization, the

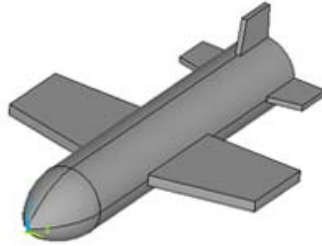


Figure 18. Geometry model of a plane-like object.

incident wave comes from the nose of this plane, i.e., $\theta = 90^\circ$, $\varphi = 0^\circ$. Table 3 shows the computation parameters of MoM and MLFMA for this example. The number of unknowns is only 23166 when PE bases are employed because the length of curvilinear triangles is about 1λ . However, it generates over 0.9 million unknowns when conventional CRWG bases are used to discretize this target. By choosing the threshold as 0.005, the percentage of zero elements reaches 78.64%, leading to a large memory saving. Actually, the memory can be saved as much as 5 times compared with MLFMA even MoM with PE bases is used. And 4.3 times CPU time saving is achieved by the reduction of unknowns and the prediction technique.

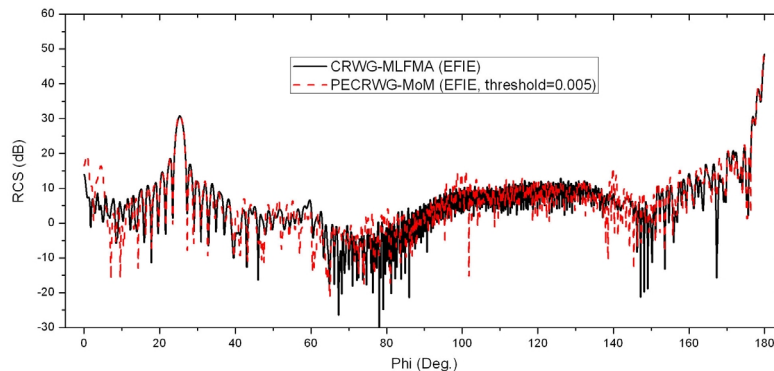


Figure 19. Bistatic RCS of a plane-like object. The frequency is 3.0 GHz and electrical length of the object is 110λ . HH -polarized.

Figure 19 is the RCS comparison between the result from non-extracted MLFMA and phase-extracted MoM, which are shown in black solid line and red dashed line, respectively. It is the most rigorous test for this target under the incident wave coming from the nose

direction and polarization direction parallel to the geometry edges, because very strong edge current can be generated at these geometry edges under such excitation condition. But the presented approach does not depress us. Appreciable errors only occur at angles about 0° , 100° , 140° and their counterparts. The differences between these two results may come from (a) The boundary current singularity, which could be overcome by use of TL or LL bases on the patches with the edges of the wings [33, 34], and (b) The lack of definition of surface wave. However, even in this engineering object, the homogeneous solution can be neglected, while the inhomogeneous solution is still dominant and gives satisfactory results. Except those differences, the solid line and dashed line match well, showing the good accuracy of PE bases and the high efficiency of the matrix sparsification technique and the impedance element prediction technique.

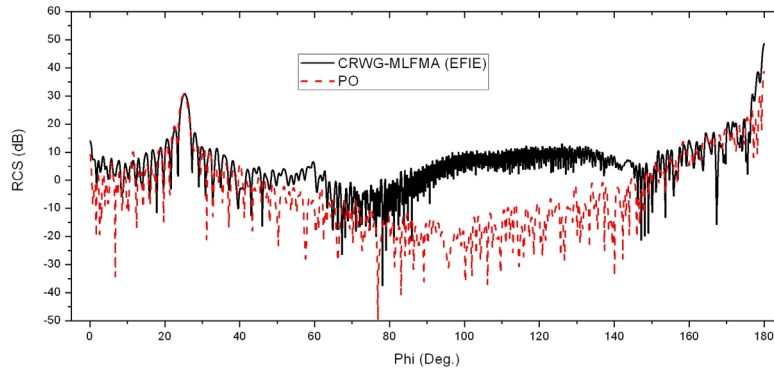


Figure 20. Result for comparison. The red dashed line is obtained from the PO method.

Table 3. Comparison of computational data for Figure 19.

Plane-Like ($f = 3.0$ GHz) (EFIE)	Unknown	Sparsity (%) / Threshold	Total Iteration Step	Total Memory Requirement (Mb)	Total Computational Time (hr.)
PE-MoM	23,166	78.64 / 0.005	299	1,315.85	94.29
CRWG-MLFMA	910,758	—	321	6,677.38	405.11
Improvement Ratio	39.31	—	—	5.07	4.30

Figure 20 shows the result from physical optics for comparison. Obviously, there are big differences at the angle range from 40° to 150° , and its counterpart from 210° to 320° . Significant error even occurred at the highest peak at 180° and its neighborhood.

6. DISCUSSIONS AND SUMMARY

It is well known that the properly designed basis functions should have their capability to describe any possible complicated distribution of the induced current on the scatterer. The traditional sub-domain bases, such as RWG or roof-top bases, have their capability through fine-meshing of the definition domain for discretely expanding of the current, and the high order hierarchical bases maintain their capability by the oscillating property of the bases for showing the standing wave distribution in their definition domain, both leading to remarkable number of the unknowns. However the PE bases gain their capability through describing the traveling wave phase dependence of the induced current, leading to much less unknown numbers.

The basis functions with the traveling wave phase dependence (PE bases) have some important advantages in MoM analysis. First, the use of PE bases results in the dramatic reduction of the number of unknowns required. Second, the impedance matrix produced by use of the PE bases can be sparsified, the same as all bases defined on the patch with electrically large size (larger than 1.5λ , for example) because of their stronger (transmission or receiving) directivities, which leads to dramatic reduction of the memory requirement. Thirdly, the phase-extracted basis functions described the intrinsic property of the induced current on the PEC surface, i.e., the traveling wave phase dependence, which ensures the well conditioning of the impedance matrix and fast convergence of the iterative solution. Furthermore, the PE bases have the excellent characteristics for wide band analysis because the bases include the frequency (phase) factor. Finally, the PE bases result in efficient interpolation in angular domain; because the amplitude factor of PE bases varies slowly while the incident (or scattering) angle changes. All these abilities are very valuable for solutions of electrically large problems, particularly for electrically large scatterer with smooth convex surface. The detailed results have not been reported here due to space limitation.

On the other hand, use of PE bases also causes some inconveniences. It is clear that the PE bases defined on the large patch fail to express the current singularity at the edges of the scatterer, similar to the other bases defined on the large patch, such as the high order bases. This difficulty can be overcome by partially adding

some appropriate bases on the fine patches including the edges [33, 34]. Moreover, the PE bases cannot be defined on large patches with the size up to 2.0λ for some structure with strong multiple scattering, such as cavity or concave structure. In this case the amplitude distribution of the current is so complex that the amplitude factor of the PE bases cannot be defined on the large patches. Finally, the use of PE bases did not result in very accurate solution in the direction tangential to almost the whole surface of the target because of the phase accuracy. However, the efficient interpolation in angular domain with PE bases surmounts this difficulty sufficiently. Therefore, the above inconveniences cannot annul the strong advantages of the PE bases.

Using the matrix sparsification technique and the impedance prediction technique of PE basis functions, the Method of Moments is greatly improved. The following three aspects of efforts contribute to the improvement of Moment Method:

- (1) The use of phase extracted basis functions reduce the number of unknowns dramatically, which is the most essential improvement in the Integral Equation Method, leading to the saving of both storage requirement and CPU time (mainly in the step of iterative solution);
- (2) Utilizing the sparse characteristic of the impedance matrix, one can obtain further reduction in memory requirement while maintaining the solution precision;
- (3) The impedance element prediction approach further reduces the computation cost greatly (both in the step of matrix formation and iterative solution).

The integrated application of these three methods makes the MoM to be even better than the MLFMA with conventional basis functions, not only in terms of the number of unknowns, but also in terms of the memory requirement and computational time.

However, the improvements presented in this paper do not change the storage and computation complexities, but only reduce N , the number of the unknowns, and the coefficient a before the complexity order N^2 . This partially leads to the less memory and CPU time savings when the electrical size goes larger. In order to alleviate the disadvantages caused by the high complexity, the PE bases can also be implemented in MLFMA. This work can be found in our further paper. On the other hand, although the complexity remains unchanged, the Method of Moments has still been improved so dramatically that it can solve electrically extra large problems even over 100λ with much lower computational spending compared with MLFMA in the given precision.

7. CONCLUSION

In this paper, the phase dependence of induced sources on PEC surfaces is deduced rigorously from electromagnetic theory. According to the derivation, basis functions with the phase factor, i.e., the phase extracted basis functions have been presented. It has been proved that the phase extraction basis functions satisfy the condition of the current continuity and are absence of charge accumulation. Describing the phase variation of the induced current successfully, the PE bases can be defined on electrically large patches with the size up to 1.5λ – 2.0λ and even larger, resulting in the dramatic reduction of the number of unknowns in MoM solution for the scattering from electrically large complex objects. Using a matrix sparsification technique and an impedance element prediction technique developed in this paper, the Method of Moments is able to solve scattering problems from electrically extra large complex targets with much lower cost than traditional MLFMA in high accuracy. With approaches presented in this paper, the Method of Moments is no longer the “low frequency method”, but can be applied in computations of many challenging real world problems (scattering from electrically large and extra large complex 3D objects, for example) with high efficiency and satisfactory accuracy.

ACKNOWLEDGMENT

The authors wish to acknowledge Prof. W. C. Chew and Prof. Q. H. Liu for valuable discussions and suggestions. This work was supported partially by National Natural Science Foundation of China under Contract No. 60431010, and 973 Program under Contract No. 6136001, partially by the 111 project under Contract No. B07046.

APPENDIX A.

In this part, Gauss divergence theorem is used to prove that the phase extracted basis functions are free of charge accumulation.

To obtain this result, it should only be proved that the net charge on the support of PE-CRWG basis functions is zero, i.e.:

$$Q = \int_S \rho(\mathbf{r}) d\mathbf{r} = 0 \quad (\text{A1})$$

where ρ stands for the charge density on the curvilinear triangular patch and S is the support of PE-CRWG basis functions. From

condition of current continuity:

$$\nabla \cdot \mathbf{J}(\mathbf{r}) = i\omega\rho(\mathbf{r}) \quad (\text{A2})$$

and substituting (A2) into (A1), one obtain:

$$Q = \frac{1}{i\omega} \int_S \nabla \cdot \mathbf{J}(\mathbf{r}) d\mathbf{r} = \frac{1}{i\omega} \int_S \nabla \cdot (\mathbf{j}e^{ik\hat{\mathbf{k}}^i \cdot \mathbf{r}}) d\mathbf{r} \quad (\text{A3})$$

Gauss divergence theorem in the 2D case is:

$$\int_S \nabla \cdot \mathbf{R} dS = \int_l \mathbf{R} \cdot d\mathbf{S} = \int_l \mathbf{R} \cdot \hat{\mathbf{n}} dl \quad (\text{A4})$$

where l is the contour of spatial surface S , $\hat{\mathbf{n}}$ is the unit normal vector of l , R has continuous partial derivative on $S \cup l$.

In order to prove that (A3) is equal to zero, two cases need to be discussed.

A.1. Without Boundary Edge

As shown in Figure A1, if these two curvilinear triangles T^+ and T^- have continuous derivatives across their common edge l^c , which means there is no boundary edge in the whole support of the basis functions, the PE-CRWG has continuous partial derivative on the surfaces and their contours. Therefore, the Gauss divergence theorem can be directly used on the whole domain:

$$\begin{aligned} Q &= \frac{1}{i\omega} \int_S \nabla \cdot (\mathbf{j}e^{ik\hat{\mathbf{k}}^i \cdot \mathbf{r}}) d\mathbf{r} = \frac{1}{i\omega} \oint_l \hat{\mathbf{n}} \cdot \mathbf{j}e^{ik\hat{\mathbf{k}}^i \cdot \mathbf{r}} dl \\ &= \frac{1}{i\omega} \left(\int_{l_1^+} \hat{\mathbf{n}} \cdot \mathbf{j}e^{ik\hat{\mathbf{k}}^i \cdot \mathbf{r}} dl + \int_{l_2^+} \hat{\mathbf{n}} \cdot \mathbf{j}e^{ik\hat{\mathbf{k}}^i \cdot \mathbf{r}} dl \right. \\ &\quad \left. + \int_{l_1^-} \hat{\mathbf{n}} \cdot \mathbf{j}e^{ik\hat{\mathbf{k}}^i \cdot \mathbf{r}} dl + \int_{l_2^-} \hat{\mathbf{n}} \cdot \mathbf{j}e^{ik\hat{\mathbf{k}}^i \cdot \mathbf{r}} dl \right) \quad (\text{A5}) \end{aligned}$$

Noticing that, on each edge of these two triangles (l_1^+ , l_1^- , l_2^+ , l_2^-), the direction of current is normal to the unit normal vector $\hat{\mathbf{n}}$, the

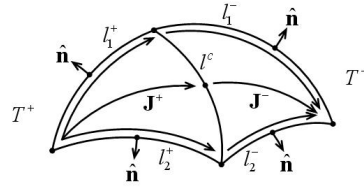


Figure A1. The definition domain of a PE-CRWG basis function.

four integrals turn out to be zero. Hence, the net charge on domain $T^+ \cup T^-$:

$$Q = 0 \quad (\text{A6})$$

A.2. With Boundary Edge

On the other hand, if there does exist a boundary edge when the two curvilinear triangles T^+ and T^- have discontinuous derivative across their common edge l^c , the PE-CRWG basis functions do not have continuous partial derivative while crossing l^c . Under this situation, the Gauss divergence theorem cannot be used directly on the whole domain $T^+ \cup T^-$, but can also be used on the separate domain T^+ and T^- :

$$\begin{aligned} Q &= \frac{1}{i\omega} \int_S \nabla \cdot (\mathbf{j}e^{ik\hat{\mathbf{k}}^i \cdot \mathbf{r}}) d\mathbf{r} \\ &= \frac{1}{i\omega} \left(\oint_{\partial T^+} \hat{\mathbf{n}} \cdot \mathbf{j}e^{ik\hat{\mathbf{k}}^i \cdot \mathbf{r}} dl + \oint_{\partial T^-} \hat{\mathbf{n}} \cdot \mathbf{j}e^{ik\hat{\mathbf{k}}^i \cdot \mathbf{r}} dl \right) \\ &= \frac{1}{i\omega} \left(\int_{l_1^+} \hat{\mathbf{n}} \cdot \mathbf{j}e^{ik\hat{\mathbf{k}}^i \cdot \mathbf{r}} dl + \int_{l_2^+} \hat{\mathbf{n}} \cdot \mathbf{j}e^{ik\hat{\mathbf{k}}^i \cdot \mathbf{r}} dl + \int_{l^c \in T^+} \hat{\mathbf{n}} \cdot \mathbf{j}e^{ik\hat{\mathbf{k}}^i \cdot \mathbf{r}} dl \right. \\ &\quad \left. + \int_{l^c \in T^-} \hat{\mathbf{n}} \cdot \mathbf{j}e^{ik\hat{\mathbf{k}}^i \cdot \mathbf{r}} dl + \int_{l_1^-} \hat{\mathbf{n}} \cdot \mathbf{j}e^{ik\hat{\mathbf{k}}^i \cdot \mathbf{r}} dl + \int_{l_2^-} \hat{\mathbf{n}} \cdot \mathbf{j}e^{ik\hat{\mathbf{k}}^i \cdot \mathbf{r}} dl \right) \quad (\text{A7}) \end{aligned}$$

where ∂T^+ and ∂T^- are the contours of triangles T^+ and T^- , respectively.

Based on the same reason that the current direction is normal to $\hat{\mathbf{n}}$, (A7) can be simplified to obtain:

$$Q = \frac{1}{i\omega} \left(\int_{l^c \in T^+} \hat{\mathbf{n}} \cdot \mathbf{j}e^{ik\hat{\mathbf{k}}^i \cdot \mathbf{r}} dl + \int_{l^c \in T^-} \hat{\mathbf{n}} \cdot \mathbf{j}e^{ik\hat{\mathbf{k}}^i \cdot \mathbf{r}} dl \right) \quad (\text{A8})$$

From the definition of phase extracted CRWG basis functions, it is simple to discover that $\hat{\mathbf{n}} \cdot \mathbf{j}e^{ik\hat{\mathbf{k}}^i \cdot \mathbf{r}}$ has the same amplitude but opposite sign since $\mathbf{j}e^{ik\hat{\mathbf{k}}^i \cdot \mathbf{r}}$ is continuous across l^c . Therefore, the same result is obtained:

$$Q = 0 \quad (\text{A9})$$

From these discussions, the conclusion that PE-CRWG basis functions are free of charge accumulation is proved.

REFERENCES

1. Hatamzadeh-Varmazyar, S., M. Naser-Moghadasi, and Z. Masouri, "A moment method simulation of electromagnetic scatter-

- ing from conducting bodies,” *Progress In Electromagnetics Research*, PIER 81, 99–119, 2008.
2. Wang, S., X. Guan, D. Wang, X. Ma, and Y. Su, “Electromagnetic scattering by mixed conducting/dielectric objects using higher order MOM,” *Progress In Electromagnetics Research*, PIER 66, 51–63, 2006.
 3. Li, C. and Z. Shen, “Electromagnetic scattering by a conducting cylinder coated with metamaterials,” *Progress In Electromagnetics Research*, PIER 42, 91–105, 2003.
 4. Yuan, H. W., S. X. Gong, X. Wang, and W. T. Wang, “Scattering analysis of a printed dipole antenna using PBG structures,” *Progress In Electromagnetics Research B*, Vol. 1, 189–195, 2008.
 5. Varmazyar, S. H. and M. N. Moghadasi, “An integral equation modeling of electromagnetic scattering from the surfaces of arbitrary resistance distribution,” *Progress In Electromagnetics Research B*, Vol. 3, 157–172, 2008.
 6. Varmazyar, S. H. and M. N. Moghadasi, “New numerical method for determining the scattered electromagnetic fields from thin wires,” *Progress In Electromagnetics Research B*, Vol. 3, 207–218, 2008.
 7. Song, J. M., C. C. Lu, and W. C. Chew, “Multilevel fast multipole algorithm for electromagnetic scattering by large complex objects,” *IEEE Trans. Antennas Propagat.*, Vol. 45, No. 10, 1488–1493, Oct. 1997.
 8. Engheta, N., W. D. Murphy, V. Rokhlin, et al., “The Fast Multipole Method (FMM) for electromagnetic scattering problems,” *IEEE Trans. Antennas Propagat.*, Vol. 40, No. 6, 634–641, 1992.
 9. Lu, C. C. and W. C. Chew, “Fast algorithm for solving hybrid integral equations,” *IEE Proceedings-H*, Vol. 140, No. 6, 455–460, 1993.
 10. Song, J. M. and W. C. Chew, “Fast multipole method solution using parametric geometry,” *Microwave and Optical Technology Letters*, Vol. 7, No. 16, 760–765, 1994.
 11. Chew, W. C., J. M. Jin, E. Michielssen, and J. M. Song, *Fast and Efficient Algorithms in Computational Electromagnetics*, Ch. 3, Artech House, Boston, 2001.
 12. Rui, P. L., R. S. Chen, Z. W. Liu, and Y. N. Gan, “Schwarz-Krylov subspace method for MLFMM analysis of electromagnetic wave scattering problems,” *Progress In Electromagnetics Research*, PIER 82, 51–63, 2008.

13. Zhang, Y. J. and E. P. Li, "Fast multipole accelerated scattering matrix method for multiple scattering of a large number of cylinders," *Progress In Electromagnetics Research*, PIER 72, 105–126, 2007.
14. Wan, J. X., T. M. Xiang, and C. H. Liang, "The fast multipole algorithm for analysis of large-scale microstrip antenna arrays," *Progress In Electromagnetics Research*, PIER 49, 239–255, 2004.
15. Pan, Y. C. and W. C. Chew, "A fast multipole method for embedded structure in a stratified medium," *Progress In Electromagnetics Research*, PIER 44, 1–38, 2004.
16. Jorgensen, E., J. L. Volakis, P. Meincke, and O. Breinbjerg, "Higher order hierarchical Legendre basis functions for iterative integral equation solvers with curvilinear surface modeling," *IEEE Antennas and Propagation Society International Symposium*, Vol. 4, 618–621, June 2002.
17. Jorgensen, E., J. L. Volakis, P. Meincke, and O. Breinbjerg, "Higher order hierarchical Legendre basis functions for electromagnetic modeling," *IEEE Trans. Antennas Propagat.*, Vol. 52, No. 11, 2985–2995, Nov. 2004.
18. Altman, Z. and R. Mittra, "Combining an extrapolation technique with the method of moments for solving large scattering problems involving bodies of revolution," *IEEE Trans. Antennas Propagat.*, Vol. 44, 548–553, Apr. 1996.
19. Altman, Z. and R. Mittra, "A technique for extrapolating numerically rigorous solutions of electromagnetic scattering problems to higher frequencies and their scaling properties," *IEEE Trans. Antennas Propagat.*, Vol. 47, No. 4, 744–751, Apr. 1999.
20. Kwon, D. H., R. J. Burkholder, and P. H. Pathak, "Efficient method of moments formulation for large pec scattering problems using Asymptotic Phasefront Extraction (APE)," *IEEE Trans. Antennas Propagat.*, Vol. 49, No. 4, 583–591, Apr. 2001.
21. Aberegg, K. R. and A. F. Peterson, "Application of the integral equation-asymptotic phase method to two-dimensional scattering," *IEEE Trans. Antennas Propagat.*, Vol. 43, 534–537, May 1995.
22. Kowalski, M. E., B. Singh, L. C. Kempel, K. D. Trott, and J.-M. Jin, "Application of the integral equation asymptotic phase (IE-AP) method to three-dimensional scattering," *J. of Electromagn. Waves and Appl.*, Vol. 15, 885–900, July 2001.
23. Taboada, J. M., F. Obelleiro, J. L. Rodriguez, I. Garcia-Tunon, and L. Landesa, "Incorporation of linear-phase progression in RWG basis functions," *Microwave and Optical Technology Letters*,

- Vol. 44, No. 2, 106–112, January 2005.
24. Abboud, T., J. C. Nedelec, and B. Zhou, “Improvement of the integral equation method for high frequency problems,” *Third International Conference on Mathematical Aspects of Wave Propagation, SIAM*, 178–187, 1995.
 25. Aberegg, K. R., “Electromagnetic scattering using the integral equation - asymptotic phase method,” Ph.D. dissertation, Georgia Institute of Technology, 1995.
 26. Shen, X., A. W. Davis, K. R. Aberegg, and A. F. Peterson, “Highly parallel implementation of the 3D integral equation asymptotic phase method for electromagnetic scattering,” *Applied Computational Electromagnetics Society (ACES) Journal*, Vol. 13, 107–115, July 1998.
 27. Darrigrand, E., “Coupling of fast multipole method and microlocal discretization for the 3-D Helmholtz equation,” *J. Computational Physics*, Vol. 181, 126–154, 2002.
 28. Graglia, R. D., D. R. Wilton, and A. F. Peterson, “Higher order interpolatory vector bases for computational electromagnetics,” *IEEE Trans. Antennas Propagat.*, Vol. 45, No. 3, 329–342, Mar. 1997.
 29. Wilkes, D. L. and C. C. Cha, “Method of moments solution with parametric curved triangular patches,” *Antennas and Propagation Society International Symposium*, Vol. 3, 1512–1515, June 1991.
 30. Zhu, N. Y. and F. M. Landstorfer, “Application of curved parametric triangular and quadrilateral edge elements in the moment solution of the EFIE,” *IEEE Microwave and Guided Wave Letters*, Vol. 3, No. 9, 319–321, Sept. 1993.
 31. Brown, W. J. and D. R. Wilton, “Singular basis functions and curvilinear triangles in the solution of the electric field integral equation,” *IEEE Trans. Antennas Propagat.*, Vol. 47, No. 2, 347–353, Feb. 1999.
 32. Wagner, R. L. and W. C. Chew, “A study of wavelets for the solution of electromagnetic integral equations,” *IEEE Trans. Antennas Propagat.*, Vol. 43, No. 8, 802–810, Aug. 1995.
 33. Yan, S. and Z. Nie, “A novel mixed basis function for method of moment,” *Proceedings of Asia-Pacific Microwave Conference 2005*, Vol. 3, Suzhou, China, Dec. 4–7, 2005.
 34. Ergül, Ö. and L. Gürel, “Linear-linear basis functions for MLFMA solutions of magnetic-field and combined-field integral equations,” *IEEE Trans. Antennas Propagat.*, Vol. 55, No. 4, 1103–1110, Apr. 2007.